



Extreme events driving year-to-year differences in gross primary productivity across the US

Alexander J. Turner¹, Philipp Köhler², Troy S. Magney³, Christian Frankenberg^{2,4}, Inez Fung⁵, and Ronald C. Cohen^{5,6}

¹Department of Atmospheric Sciences, University of Washington, Seattle, WA, 98195, USA

²Division of Geological and Planetary Sciences, California Institute of Technology, Pasadena, CA, 91226, USA.

³Department of Plant Sciences, University of California, Davis, CA, 95616, USA.

⁴Jet Propulsion Laboratory, California Institute of Technology, Pasadena, CA, 91109, USA.

⁵Department of Earth and Planetary Sciences, University of California, Berkeley, CA, 94720, USA.

⁶College of Chemistry, University of California, Berkeley, CA, 94720, USA.

Correspondence: Alexander J. Turner (turneraj@uw.edu)

1 **Abstract.** Solar-Induced chlorophyll Fluorescence (SIF) has previously been shown to strongly correlate with gross primary
2 productivity (GPP), however this relationship has not yet been quantified for the recently launched TROPospheric Monitoring
3 Instrument (TROPOMI). Here we use a Gaussian mixture model to develop a parsimonious relationship between SIF from
4 TROPOMI and GPP from flux towers across the conterminous United States (CONUS). The mixture model indicates the
5 SIF-GPP relationship can be characterized by a linear model with two terms. We then estimate GPP across CONUS at 500-m
6 spatial resolution over a 16-day moving window. We find that CONUS GPP varies by less than 4% between 2018 and 2019.
7 However, we observe four extreme precipitation events that induce regional GPP anomalies: drought in west Texas, flooding in
8 the midwestern US, drought in South Dakota, and drought in California. Taken together, these events account for 28% of the
9 year-to-year GPP differences across CONUS.

10 1 Introduction

11 Terrestrial gross primary productivity (GPP) is the total amount of carbon dioxide (CO₂) assimilated by plants through pho-
12 tosynthesis and represents one of the main drivers of interannual variability in the global carbon cycle Le Quéré et al. (2018).
13 As such, quantifying the spatiotemporal patterns of terrestrial GPP is critical to understanding how the carbon cycle will both
14 respond to and influence climate. Work over the past decade has shown satellite measurements of solar-induced chlorophyll
15 fluorescence (SIF) to correlate strongly with tower-based estimates of GPP (e.g., Frankenberg et al., 2011; Yang et al., 2015;
16 Sun et al., 2017; Turner et al., 2020; Wang et al., 2020) and are often used as a remote-sensing proxy for GPP.

17 This relationship between SIF and GPP is typically expressed through a pair of light use efficiency models Monteith (1972)
18 that relate GPP and SIF to the absorbed photosynthetically active radiation (APAR):

$$19 \text{ GPP} = \text{APAR} \times \Phi_{\text{CO}_2} \quad (1)$$

$$20 \text{ SIF} = \text{APAR} \times \beta \Phi_{\text{F}} \quad (2)$$



1 where Φ_{CO_2} is the light use efficiency of CO_2 assimilation, Φ_{F} is the fluorescence yield, and β is the probability of fluoresced
2 photons escaping the canopy. Solving for APAR and substituting, we can rewrite GPP as:

$$3 \text{ GPP} = \frac{\Phi_{\text{CO}_2}}{\beta\Phi_{\text{F}}} \text{SIF}. \quad (3)$$

4 The derivation follows from Lee et al. (2013), Guanter et al. (2014), Sun et al. (2017), and others.

5 This seemingly straightforward relationship between SIF and GPP has been widely used to infer GPP from measurements of
6 SIF (e.g., Frankenberg et al., 2011; Parazoo et al., 2014; Yang et al., 2015, 2017; Sun et al., 2017, 2018; Magney et al., 2019;
7 Turner et al., 2020) with some work showing that SIF captures more variability in GPP than APAR alone (e.g., Yang et al.,
8 2015, 2017; Magney et al., 2019). However, there is much complexity encapsulated in the first term of Eq. 3 ($\Phi_{\text{CO}_2}/\beta\Phi_{\text{F}}$).
9 There is an ongoing debate about what *exactly* SIF is telling us about GPP (e.g., Joiner and Yoshida, 2020; Maguire et al., 2020;
10 Dechant et al., 2020; He et al., 2020; Marrs et al., 2020) and the spatio-temporal scales at which SIF and GPP correlate well. A
11 recent paper from Magney et al. (2020) presents a concise summary of the covariation between SIF and GPP at different spatio-
12 temporal scales and how non-linear relationships at the leaf-scale often integrate to a linear response at the canopy-scale. This
13 is due, in large part, to the fact that most of our satellite measurements occur near the middle of the day when the Φ_{CO_2} - Φ_{F}
14 response is more-or-less linear and the observed signal is integrated over many leaves.

15 Here we focus on the ecosystem-scale relationship between SIF and GPP, as that is the relevant observable scale from space-
16 borne instruments. We begin by characterizing the relationship between instantaneous SIF from TROPOMI and half-hourly
17 GPP from flux towers. Following this, we use this ecosystem-scale relationship to infer GPP at a spatial resolution of 500-m
18 using TROPOMI SIF measurements and identify drivers of interannual variability in GPP. Previous work has identified effects
19 such as seasonal redistribution Butterfield et al. (2020), drought (e.g., Sun et al., 2015), and flooding Yin et al. (2020) as
20 important drivers of interannual variability in GPP.

21 **2 Identifying distinct relationships between SIF and GPP**

22 We build on our previous work Turner et al. (2020) downscaling measurements of SIF to 500-m spatial resolution. Briefly, the
23 TROPospheric Monitoring Instrument (TROPOMI; Veefkind et al., 2012) is a nadir-viewing imaging spectrometer. TROPOMI
24 has a 2,600 km swath with a nadir spatial resolution of 5.6 km along track and 3.5 km across track. Köhler et al. (2018) presented
25 the first retrievals of SIF from TROPOMI. As in Turner et al. (2020), we apply a *post hoc* bias correction to ensure positivity
26 of monthly average values as systematically negative SIF values are non-physical. We downscale individual TROPOMI scenes
27 using the near-infrared reflectance of vegetation index (NIR_v) that was proposed by Badgley et al. (2017, 2019). We use
28 the MCD43A4.006 (v06) MODIS NBAR reflectances Schaaf et al. (2002) to compute NIR_v . Two notable differences from
29 Turner et al. (2020) are: 1) the analysis is extended to cover all of CONUS and 2) we now use a 16-day moving window, thus
30 including a full orbit cycle in each averaging window to minimize effects due to viewing-illumination geometry and noise.
31 Supplemental Fig. S3 shows the improvement when averaging to longer temporal windows with an r of 0.66, 0.74, 0.79, and
32 0.82 for instantaneous, 8-day, 16-day, and 32-day temporal windows, respectively.

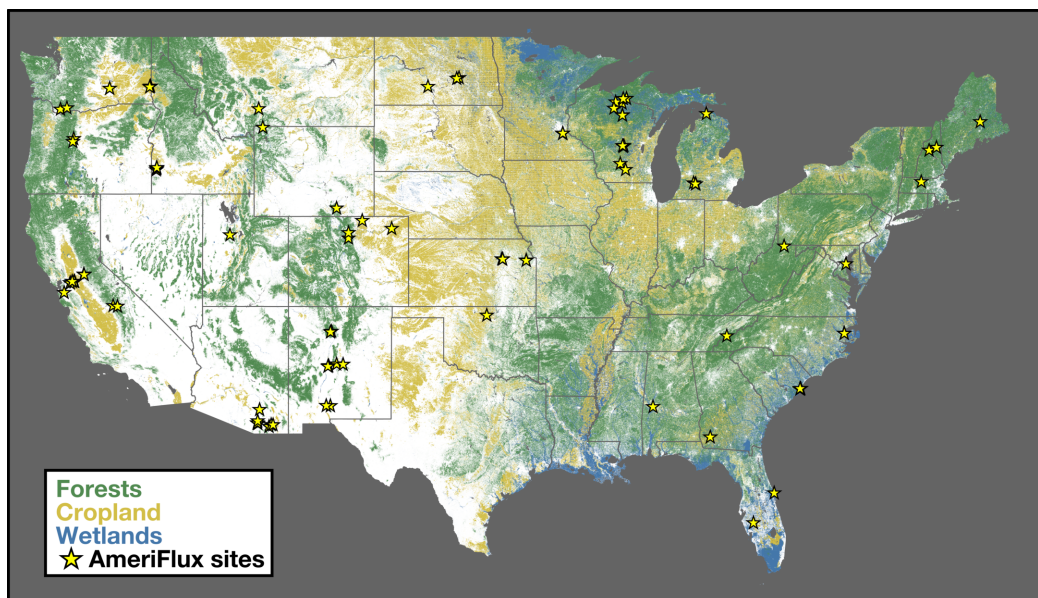


Figure 1. Dominant landcover over conterminous United States (CONUS). Colors show the dominant landcover over CONUS. Classification is based on the 2019 USDA CropScape database USDA (2018). Forests are shown in green croplands in yellow, and wetlands in blue. Location of 82 AmeriFlux sites used in this study are shown as yellow stars.

1 The extension to CONUS facilitates comparison of TROPOMI SIF retrievals to flux tower data over a more representative
2 set of ecosystems and robustly infer the SIF-GPP relationship. Specifically, there are 82 AmeriFlux sites Baldocchi et al. (2001)
3 within CONUS that reported data in 2018, 2019, or 2020 whereas Turner et al. (2020) only included 11 sites and did not have
4 data from forests. Figure 1 shows the location of these 82 AmeriFlux sites overlaid on the dominant landcover. These eddy
5 covariance sites provide a direct measure of net ecosystem exchange (NEE; CO₂ fluxes) Baldocchi et al. (1988). We use GPP
6 that has been partitioned by the group operating the site. If GPP is not provided we compute it using nighttime measurements
7 of NEE as a proxy for ecosystem respiration Reichstein et al. (2005). The AmeriFlux sites used here cover 10 ecosystems as
8 defined by the International Geosphere-Biosphere Programme: evergreen needleleaf forest, deciduous broadleaf forest, mixed
9 forest, grassland, cropland, wetland, woody savanna, savanna, open shrubland, and closed shrubland.

10 We characterize the relationship between TROPOMI SIF and AmeriFlux GPP by plotting downscaled instantaneous SIF
11 observations against the nearest AmeriFlux GPP data in time (see Supplemental Figs. S1-S3). Specifically, the 6 steps we
12 take here are: 1) apply the *post hoc* bias correction to the TROPOMI SIF data, 2) find all TROPOMI scenes that cover an
13 AmeriFlux site, 3) downscale TROPOMI scenes to 500-m using MODIS NIR_v, 4) construct a timeseries of SIF observations
14 from the 500-m grid cell that contains the AmeriFlux site, 5) construct a timeseries of AmeriFlux GPP data that are coincident
15 in time with the TROPOMI overpass, and 6) regress SIF on GPP with a bisquare regression. The bisquare regression was
16 chosen due to robustness against outliers. Additionally, we force the regression through the origin based on the physical
17 constraint that GPP should be zero if SIF is zero. We observe a linear relationship between SIF and GPP when plotted against



1 all ecosystems (Supplemental Figure S1) and when separated by ecosystem (Supplemental Figure S2). Notable exceptions
2 are closed shrubland, open shrubland, and savanna ecosystems where SIF explains less than 10% of the variability in GPP
3 for AmeriFlux sites in those ecosystems due, in part, to a low signal-to-noise ratio. These ecosystems typically have a small
4 signal and the bright surfaces often result in a higher retrieval uncertainty. This combination of a small signal and high retrieval
5 uncertainty results in a low signal-to-noise ratio, complicating efforts to derive a robust relationship between SIF and GPP for
6 these ecosystems.

7 Many of the ecosystems exhibit a similar linear relationship between SIF and GPP, which begs the question: “*what ecosys-*
8 *tems have a distinct SIF-GPP relationship?*” To address this, we bootstrap the bisquare regression for each ecosystem 2000
9 times. The slopes from this bootstrap can be seen in Figure 2. The range of slopes vary from 13 to 18 ($\mu\text{mol m}^{-2} \text{s}^{-1}$) / ($\text{mW m}^{-2} \text{sr}^{-1} \text{s}^{-1}$)
10 with grasslands at the low end and evergreen needleleaf forests at the high end. We then use a two component Gaussian mixture
11 model (see, for example, Bishop, 2007) to identify clusters of ecosystems with a similar SIF-GPP relationship. The implemen-
12 tation of our Gaussian mixture model is adapted from Turner and Jacob (2015). Parameters of the mixture model are obtained
13 via an iterative expectation-maximization algorithm. A drawback of these mixture models is they often find local minima. To
14 address this, we repeat the fitting of the mixture model with multiple initializations and use simulated annealing to search for
15 a global minimum. We tested a range of mixture model sizes and found a mixture of two Gaussians to be the most robust. The
16 resulting mixture model is overlaid on the histogram in Figure 2.

17 We observe a clustering of ecosystems with SIF-GPP relationships around 16.4 ($\mu\text{mol m}^{-2} \text{s}^{-1}$) / ($\text{mW m}^{-2} \text{sr}^{-1} \text{s}^{-1}$). This
18 grouping is the dominant weighting term for wetlands, evergreen needleleaf forest, deciduous broadleaf forest, mixed forest,
19 cropland, and woody savanna. We refer to this cluster as the “Dominant Cluster” and assume that ecosystems not specifically
20 mentioned elsewhere will have a response that is similar to this primary cluster. The other component of the mixture model
21 corresponds to grasslands. Ecosystems not explicitly mentioned use the “Dominant Cluster” for scaling SIF to GPP. Table 1
22 lists the SIF-GPP relationships for these two clusters. Previous work has also found unique SIF-GPP relationships between C3
23 and C4 plants using measurements from a tower including a non-linear response in C3 plants He et al. (2020), we examined
24 this here using two AmeriFlux sites in corn fields and two in potato fields. We do observe potential differences in the SIF-GPP
25 relationship between these C3 and C4 systems (see Supplemental Figure S5). The difference in SIF-GPP relationship for C3
26 and C4 systems seen here is also similar to what was observed using NIR_v Badgley et al. (2019). These relationships can be
27 used to reconstruct GPP from TROPOMI SIF as: $\text{GPP} = \text{SIF} \times (\sum_i f_i s_i)$ where s_i is the SIF-GPP relationship in Table 1 for
28 the i^{th} cluster and f_i is the fraction of a grid cell represented by that cluster.

29 TROPOMI is in low earth orbit and only observes a snapshot in time. The equatorial overpass time at nadir is 13:30 local
30 time. By assuming that GPP scales linearly with PAR (i.e., Eq. 1) we can compute a correction factor to estimate daily integrated
31 GPP. More formally, we scale the instantaneous SIF by the ratio of the integral of the cosine of the solar zenith angle (SZA) over
32 the day to $\cos(\text{SZA})$ from the TROPOMI overpass time. Putting everything together, we estimate daily GPP from TROPOMI
33 SIF observations as:

34
$$\text{GPP}(x, y, t) = \text{SIF}(x, y, t) \cdot \gamma \sum_i s_i f_i(x, y) \cdot \frac{\int_{\tau_0}^{\tau_f} \cos[\text{SZA}(x, y, \tau)] d\tau}{\cos[\text{SZA}(x, y, \tau_s)]} \quad (4)$$

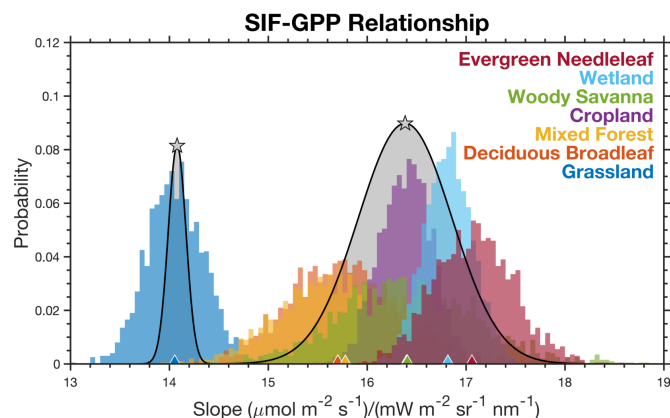


Figure 2. Identifying distinct SIF-GPP relationships across ecosystems. Histogram shows the distribution of slopes that map SIF to GPP using a bisquare regression and a 2000 member bootstrap. Colors denote the different ecosystems and triangles at the bottom show the mean for that ecosystem. Gray distributions are from a two-member Gaussian Mixture Model and the stars indicate the mean for that component.

Table 1. SIF-GPP relationships for different groupings.

Cluster	SIF-GPP relationship ^a (s_i)
Dominant Cluster	16.4 ± 0.4
Grassland	14.1 ± 0.1

^aAll SIF-GPP relationships have units of $(\mu\text{mol m}^{-2} \text{s}^{-1}) / (\text{mW m}^{-2} \text{sr}^{-1} \text{nm}^{-1})$. Uncertainty is the diagonal of the covariance matrix for the mixture model.

1 where $\text{SIF}(x, y, t)$ is the 500-m downscaled SIF using a 16-day moving window, γ is a unit conversion from μmol to gC , s_i is
 2 the SIF-GPP relationship inferred from comparison with AmeriFlux GPP (see Table 1), $f_i(x, y)$ is the fraction of the grid cell
 3 represented by the i^{th} cluster, SZA is the local solar zenith angle, τ_0 is sunrise, τ_f is sunset, and τ_s is the hour corresponding to
 4 the TROPOMI overpass time. We do not include information on cloud cover in our approach, this could potentially be included
 5 in the future to account for diurnal variations in PAR.

6 3 Drivers of interannual variations in US gross primary productivity

7 Figure 3 shows annual mean GPP across CONUS inferred from TROPOMI SIF measurements using Eq. 4. A number of
 8 prominent features are visible such as the Central Valley of California, the Snake River Valley in Idaho, and the Adirondack
 9 Mountains in upstate New York. California's Central Valley and Idaho's Snake River Valley are both major agricultural regions
 10 in the western US (e.g., the Central Valley of California accounts for more than 15% of irrigated land in the US). The Adirondack



- 1 Mountains are a roughly circular dome that rise above the surrounding lowlands, resulting in a shorter growing season and lower
- 2 annual mean GPP. This shortened growing season can be seen in an animation of GPP over CONUS (Supplemental Movie S1).

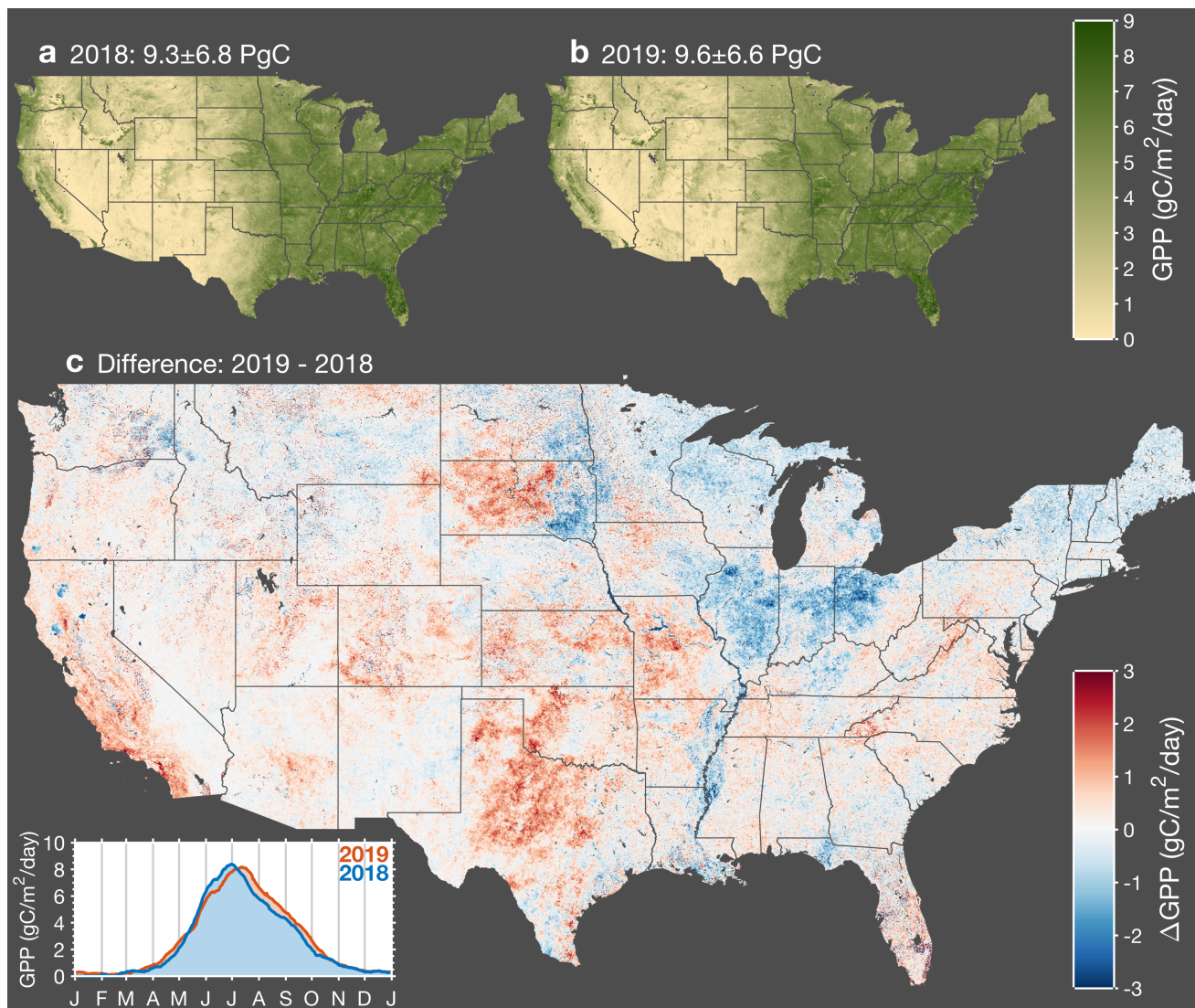


Figure 3. Interannual variations in gross primary productivity across CONUS. Map of annual mean GPP for 2018 (panel a) and 2019 (panel b). (Panel c) Map of the difference in annual mean GPP between 2019 and 2018. Red indicates higher GPP in 2019 and blue indicates higher GPP in 2018. Inset in bottom left corner shows a timeseries of the average GPP across CONUS for 2018 and 2019.

- 3 We observe substantial GPP across the eastern US (delineated here by 98°W) with annual mean values generally in excess of
- 4 $5 \text{ gC/m}^2/\text{day}$. This region accounts for less than half of the land but more than 70% of the annual GPP. This delineation in GPP
- 5 roughly coincides with the location of drylands in CONUS that are more sensitive to changes in precipitation; drylands are also



1 projected to expand in future climate Yao et al. (2020). Most of the large year-to-year differences occur in these western US
2 drylands (see Fig. 3c), a notable exception being a negative GPP anomaly in 2019 relative to 2018 that extended across Illinois,
3 Indiana, and Ohio. Here we highlight four precipitation-driven GPP anomalies, which taken together, account for 28% of the
4 interannual GPP variability across the United States: 1) 2018 drought in west Texas, 2) 2019 midwestern crop flooding, 3) 2018
5 drought in South Dakota, and 4) 2018 drought in California. Figure 4 summarizes the interannual precipitation differences that
6 we hypothesize are responsible for explaining these four GPP anomalies.

7 The largest positive GPP anomaly in 2019 relative to 2018 was observed across western Texas. This single event accounted
8 for 11% of the year-to-year difference in GPP across CONUS with an annual GPP of 0.65 ± 0.47 PgC in 2018 and $0.76 \pm$
9 0.45 PgC in 2019. From Figure 4a, we observe 50% higher GPP in spring 2019 compared to spring 2018. This increase in GPP
10 was driven by a lack of precipitation in spring 2018. The cumulative precipitation from October 2017 through June 2018 was
11 50% less than October 2018 through June 2019 (500 mm vs 1000 mm). The other notable difference between GPP in 2018 and
12 2019 was a second peak during fall 2018 that was not present in 2019. This second peak coincided with a series of precipitation
13 events beginning in early September. This tight coupling between GPP and precipitation is expected for dryland systems such
14 as west Texas (e.g., Smith et al., 2019). The seasonal GPP dynamics inferred from TROPOMI SIF are also present in the
15 MODIS vegetation index NIR_v , albeit with slight differences in magnitude, implying convergent responses in SIF and NIR_v
16 for this ecosystem.

17 The second largest anomaly is the reduction in 2019 GPP relative to 2018 across midwestern crop areas (specifically Illinois,
18 Indiana, and Ohio) that accounted for 7% of the year-to-year difference in CONUS GPP. The 2018 annual GPP was $0.70 \pm$
19 0.12 PgC and 0.63 ± 0.14 PgC in 2019. We observe a decrease in the maximum GPP between 2019 and 2018 as well as a two
20 week delay in the timing of the maximum. This anomaly was highlighted in recent work from Yin et al. (2020) who attribute
21 the anomaly to flooding in the midwestern US. The flooding delayed planting of crops by two weeks and resulted in decreased
22 carbon uptake across the midwestern crop areas and Mississippi Alluvial Valley, where we also observe a negative anomaly in
23 Figure 3c. Yin et al. (2020) provide a detailed discussion of these floods and their impacts on crop productivity.

24 South Dakota exhibits a dipole with positive anomalies in 2019 in the west and negative anomalies in the east, again relative
25 to 2018. The 2018 annual GPP was 0.20 ± 0.09 PgC and 0.63 ± 0.08 PgC in 2019. The negative anomalies in the east are
26 driven by the flooding events discussed above and in Yin et al. (2020). However, the positive anomaly in western portion of
27 the state is the dominant term. This positive anomaly is driven by a series of summer precipitation events that served to extend
28 the growing season across the western plains. From Figure 4c, we can see three precipitation events throughout the mid-to-late
29 summer that coincide with pauses in senescence: mid-July, early August, and mid-September. As with Texas, this highlights
30 the tight coupling between GPP and precipitation for dryland systems. In toto, these precipitation events served to increase
31 statewide GPP in 2019 relative to 2018.

32 The final notable anomaly is California's positive GPP anomaly in 2019. The 2018 annual GPP was 0.27 ± 0.24 PgC and
33 0.33 ± 0.26 PgC in 2019. 2018 was a mild drought in California with ~80% of the state being classified as abnormally dry;
34 2019 had 50% more precipitation during the water year than 2018 (Figure 4c). Two consequences of this drought in 2018 were:
35 a delayed onset of photosynthesis and a mid-summer senescence. The onset of photosynthesis in 2018 coincided with a series

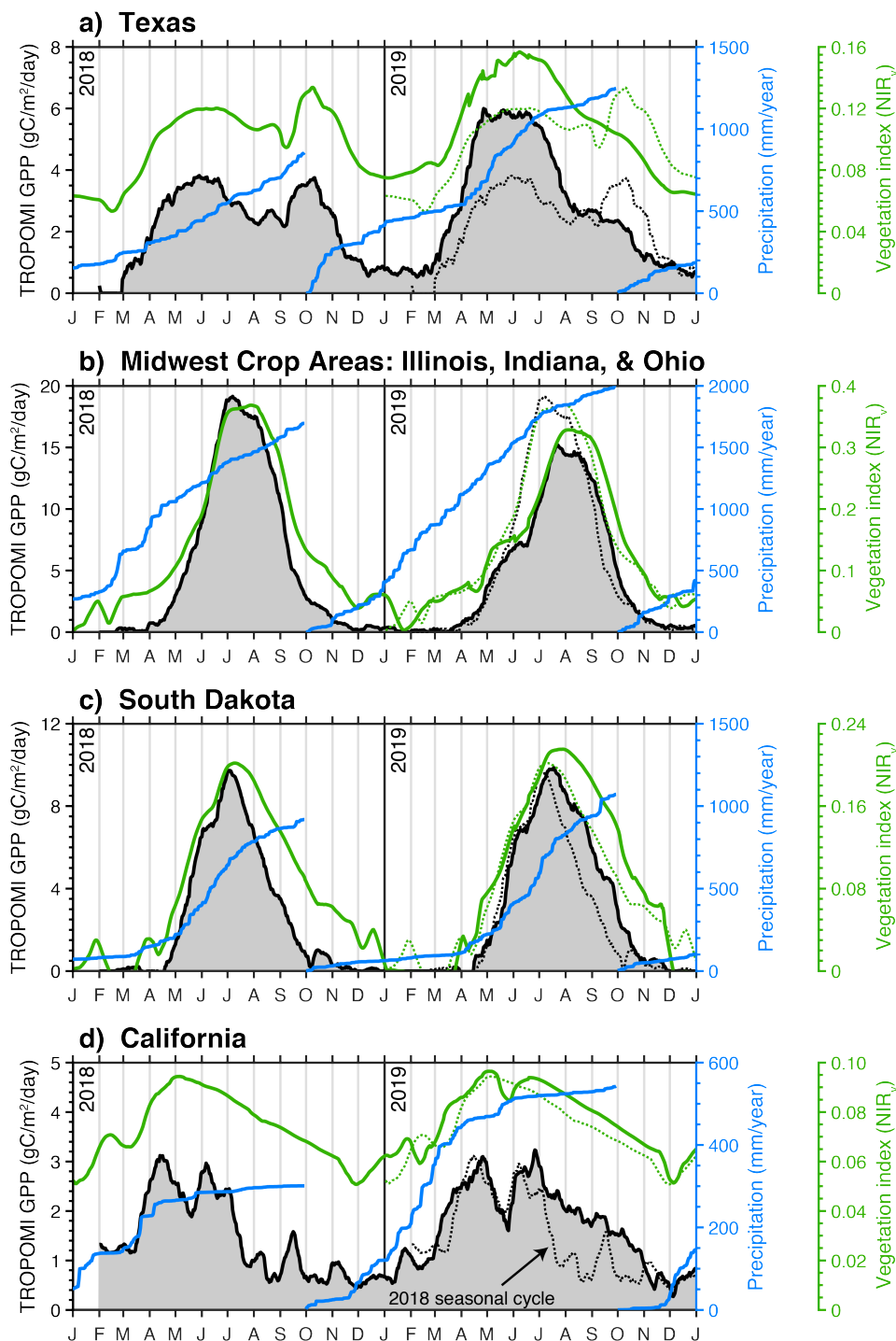


Figure 4. Major drivers of interannual variability in CONUS GPP. Black line shows the TROPOMI-derived GPP over Texas (a), the midwest crop region (b), South Dakota (c), and California (d). Blue line shows the cumulative precipitation over the water year as measured by the GPM satellite. Green line is NIR_v from MODIS. Black and Green dotted lines are 2018 GPP and NIR_v superimposed on the 2019 timeseries.



1 of atmospheric rivers that delivered about a third of the total precipitation that year, indicating a water limitation up to that
2 point. In contrast, 2019 had ample precipitation through the winter and we observe both an earlier onset of photosynthesis and
3 an extension of the growing season into the fall. Evergreen forests are the main contributor to the SIF signal during the summer
4 and fall Turner et al. (2020) and, as such, will be more sensitive to the accumulated precipitation. The spatial pattern of the
5 differences in August–November GPP (Fig. S4) strongly correlate with evergreen forests.

6 In contrast to the anomalies presented earlier, the SIF-derived GPP and MODIS-based vegetation index (NIR_v) show di-
7 vergent seasonal dynamics for California. NIR_v shows small differences between 2018 and 2019 with a strong similarity to
8 the 2019 SIF-derived GPP. The seasonality of NIR_v is similar to that of the leaf area index (LAI) derived from MODIS (see
9 Supplemental Figure 6), implying a biophysical signal. Vegetation indices estimate *photosynthetic capacity* provided optimal
10 soil moisture, temperature, and PAR are known Sellers (1985). As such, this suggests that we observed a down-regulation of
11 photosynthesis from evergreen forests in response to a water limitation during fall 2018, whereas these forests were close to
12 photosynthetic capacity in fall 2019 resulting in a similar seasonality to 2018 and 2019 NIR_v . Sims et al. (2014) also report a
13 low sensitivity of MODIS vegetation indices to drought stress in forests.

14 4 Conclusions

15 We have developed a parsimonious relationship between measurements of SIF from TROPOMI and GPP inferred from flux
16 towers. This relationship allows for estimation of GPP directly from TROPOMI SIF measurements. We combine this SIF-
17 GPP relationship with work downscaling TROPOMI data to 500-m spatial resolution to construct estimates of GPP across the
18 conterminous United States in 2018 and 2019. Our estimate of US GPP varies by less than 4% between 2018 and 2019. We do,
19 however, observe large regional anomalies that are driven by extreme precipitation events. Namely, west Texas, South Dakota,
20 and California experienced droughts in 2018 while midwestern US crop areas (Illinois, Indiana, and Ohio) experienced flooding
21 in 2019. Taken together, these four events account for 28% of the year-to-year variability in GPP across the conterminous
22 United States.

23 The impact of the west Texas drought, South Dakota drought, and midwestern flooding are observed in other remote-
24 sensing measures of photosynthetic capacity such as NIR_v while the California drought shows a divergent result using SIF; the
25 divergent responses are driven by specific ecosystems such as evergreen forests. Our work suggests that SIF provides a measure
26 of *photosynthetic activity* as opposed to *photosynthetic capacity*, and converge with other remote-sensing measures under non-
27 stressed conditions. Future work investigating the response to extreme events across ecosystems may provide additional insight
28 into these divergent responses in remote-sensing measurements related to photosynthesis.

29 *Acknowledgements.* We are grateful to the team that has realized the TROPOMI instrument, consisting of the partnership between Airbus
30 Defence and Space, KNMI, SRON, and TNO, commissioned by NSO and ESA. We acknowledge the following AmeriFlux sites for their
31 data records: US-ALQ, US-ARM, US-Bi1, US-Bi2, US-CF1, US-CF2, US-CF3, US-CF4, US-CS1, US-CS2, US-CS3, US-EDN, US-GLE,



1 US-Hn2, US-Hn3, US-Ho1, US-JRn, US-Jo2, US-KS3, US-Los, US-Me2, US-Me6, US-Men, US-Mpj, US-MtB, US-Myb, US-NC2, US-
2 NC3, US-NC4, US-RIs, US-Rms, US-Ro4, US-Ro5, US-Ro6, US-Rwf, US-Rws, US-SRG, US-SRM, US-Seg, US-Ses, US-Sne, US-Snf,
3 US-Syv, US-Ton, US-Tw1, US-Tw4, US-Tw5, US-UMd, US-Var, US-Vcm, US-Vcp, US-WCr, US-Whs, US-Wjs, US-Wkg, US-xAB, US-
4 xBR, US-xCP, US-xDC, US-xDL, US-xHA, US-xJE, US-xJR, US-xKA, US-xKZ, US-xNG, US-xNQ, US-xRM, US-xSE, US-xSL, US-
5 xSP, US-xSR, US-xST, US-xTE, US-xUK, US-xUN, US-xWD, US-xWR, US-xYE. In addition, funding for AmeriFlux data resources was
6 provided by the U.S. Department of Energy’s Office of Science. **Funding:** AJT was supported as a Miller Fellow with the Miller Institute for
7 Basic Research in Science at UC Berkeley. This research was funded by grants from the Koret Foundation and NASA 80NSSC19K0945 for
8 support of the computational resources. Part of this research was funded by the NASA Carbon Cycle Science program (grant NNX17AE14G).
9 TROPOMI SIF data generation by PK and CF is funded by the Earth Science U.S. Participating Investigator program (grant NNX15AH95G).
10 This research used the Savio computational cluster resource provided by the Berkeley Research Computing program at the University of
11 California, Berkeley (supported by the UC Berkeley Chancellor, Vice Chancellor for Research, and Chief Information Officer). **Author**
12 **contributions:** AJT wrote the text with feedback from all authors. PK and CF performed the TROPOMI SIF retrievals. AJT downscaled
13 the SIF data, conducted the AmeriFlux analysis, and drafted the figures. All authors contributed to the discussion and analysis. **Competing**
14 **interests:** The authors declare no competing interests. **Data and materials availability:** Daily gridded 500-m TROPOMI SIF and GPP
15 data from February 1, 2018 through June 15, 2020 is temporarily available on Google Drive here: “<https://bit.ly/2GHEOOq>”, and will be
16 uploaded to the ORNL DAAC at acceptance.



1 References

- 2 Badgley, G., Field, C. B., and Berry, J. A.: Canopy near-infrared reflectance and terrestrial photosynthesis, *Sci Adv*, 3, e1602244,
3 <https://doi.org/10.1126/sciadv.1602244>, 2017.
- 4 Badgley, G., Anderegg, L. D. L., Berry, J. A., and Field, C. B.: Terrestrial Gross Primary Production: Using NIR_V to Scale from Site to
5 Globe, *Global change biology*, <https://doi.org/10.1111/gcb.14729>, 2019.
- 6 Baldocchi, D., Falge, E., Gu, L., Olson, R., Hollinger, D., Running, S., Anthoni, P., Bernhofer, C., Davis, K., Evans, R., Fuentes, J., Gold-
7 stein, A., Katul, G., Law, B., Lee, X., Malhi, Y., Meyers, T., Munger, W., Oechel, W., Paw, K. T., Pilegaard, K., Schmid, H. P., Valen-
8 tini, R., Verma, S., Vesala, T., Wilson, K., and Wofsy, S.: FLUXNET: A New Tool to Study the Temporal and Spatial Variability of
9 Ecosystem-Scale Carbon Dioxide, Water Vapor, and Energy Flux Densities, *Bulletin of the American Meteorological Society*, 82, 2415–
10 2434, [https://doi.org/10.1175/1520-0477\(2001\)082<2415:fantts>2.3.co;2](https://doi.org/10.1175/1520-0477(2001)082<2415:fantts>2.3.co;2), 2001.
- 11 Baldocchi, D. D., Hicks, B. B., and Meyers, T. P.: Measuring Biosphere-Atmosphere Exchanges of Biologically Related Gases with Microm-
12 eteorological Methods, *Ecology*, 69, 1331–1340, <https://doi.org/10.2307/1941631>, 1988.
- 13 Bishop, C. M.: *Pattern Recognition and Machine Learning*, Springer, 1 edn., 2007.
- 14 Butterfield, Z., Buermann, W., and Keppel-Aleks, G.: Satellite observations reveal seasonal redistribution of northern ecosystem productivity
15 in response to interannual climate variability, *Remote Sensing of Environment*, 242, 111 755, <https://doi.org/10.1016/j.rse.2020.111755>,
16 2020.
- 17 Dechant, B., Ryu, Y., Badgley, G., Zeng, Y., Berry, J. A., Zhang, Y., Goulas, Y., Li, Z., Zhang, Q., Kang, M., Li, J., and Moya, I.: Canopy
18 structure explains the relationship between photosynthesis and sun-induced chlorophyll fluorescence in crops, *Remote Sensing of Envi-
19 ronment*, 241, 111 733, <https://doi.org/10.1016/j.rse.2020.111733>, 2020.
- 20 Frankenberg, C., Butz, A., and Toon, G. C.: Disentangling chlorophyll fluorescence from atmospheric scattering effects in O₂A-band spectra
21 of reflected sun-light, *Geophysical Research Letters*, 38, <https://doi.org/10.1029/2010gl045896>, 2011.
- 22 Guanter, L., Zhang, Y., Jung, M., Joiner, J., Voigt, M., Berry, J. A., Frankenberg, C., Huete, A. R., Zarco-Tejada, P., Lee, J. E., Moran,
23 M. S., Ponce-Campos, G., Beer, C., Camps-Valls, G., Buchmann, N., Gianelle, D., Klumpp, K., Cescatti, A., Baker, J. M., and Griffis,
24 T. J.: Global and time-resolved monitoring of crop photosynthesis with chlorophyll fluorescence, *Proceedings of the National Academy
25 of Sciences of the United States of America*, 111, E1327–33, <https://doi.org/10.1073/pnas.1320008111>, 2014.
- 26 He, L., Magney, T., Dutta, D., Yin, Y., Köhler, P., Grossmann, K., Stutz, J., Dold, C., Hatfield, J., Guan, K., Peng, B., and Frankenberg, C.:
27 From the Ground to Space: Using Solar-Induced Chlorophyll Fluorescence to Estimate Crop Productivity, *Geophysical Research Letters*,
28 47, <https://doi.org/10.1029/2020gl087474>, 2020.
- 29 Joiner, J. and Yoshida, Y.: Satellite-based reflectances capture large fraction of variability in global gross primary production (GPP) at weekly
30 time scales, *Agricultural and Forest Meteorology*, 291, 108 092, <https://doi.org/10.1016/j.agrformet.2020.108092>, 2020.
- 31 Köhler, P., Frankenberg, C., Magney, T. S., Guanter, L., Joiner, J., and Landgraf, J.: Global Retrievals of Solar-Induced Chlorophyll Flu-
32 orescence With TROPOMI: First Results and Intersensor Comparison to OCO-2, *Geophysical Research Letters*, 45, 10,456–10,463,
33 <https://doi.org/10.1029/2018gl079031>, 2018.
- 34 Le Quéré, C., Andrew, R. M., Friedlingstein, P., Sitch, S., Hauck, J., Pongratz, J., Pickers, P. A., Korsbakken, J. I., Peters, G. P., Canadell,
35 J. G., Arneeth, A., Arora, V. K., Barbero, L., Bastos, A., Bopp, L., Chevallier, F., Chini, L. P., Ciais, P., Doney, S. C., Gkritzalis, T., Goll,
36 D. S., Harris, I., Haverd, V., Hoffman, F. M., Hoppema, M., Houghton, R. A., Hurtt, G., Ilyina, T., Jain, A. K., Johannessen, T., Jones,
37 C. D., Kato, E., Keeling, R. F., Goldewijk, K. K., Landschützer, P., Lefèvre, N., Lienert, S., Liu, Z., Lombardozi, D., Metzl, N., Munro,



- 1 D. R., Nabel, J. E. M. S., Nakaoka, S.-i., Neill, C., Olsen, A., Ono, T., Patra, P., Peregón, A., Peters, W., Peylin, P., Pfeil, B., Pierrot,
2 D., Poulter, B., Rehder, G., Resplandy, L., Robertson, E., Rocher, M., Rödenbeck, C., Schuster, U., Schwinger, J., Séférian, R., Skjelvan,
3 I., Steinhoff, T., Sutton, A., Tans, P. P., Tian, H., Tilbrook, B., Tubiello, F. N., van der Laan-Luijkx, I. T., van der Werf, G. R., Viovy,
4 N., Walker, A. P., Wiltshire, A. J., Wright, R., Zaehle, S., and Zheng, B.: Global Carbon Budget 2018, *Earth System Science Data*, 10,
5 2141–2194, <https://doi.org/10.5194/essd-10-2141-2018>, 2018.
- 6 Lee, J. E., Frankenberg, C., van der Tol, C., Berry, J. A., Guanter, L., Boyce, C. K., Fisher, J. B., Morrow, E., Worden, J. R., Asefi, S.,
7 Badgley, G., and Saatchi, S.: Forest productivity and water stress in Amazonia: observations from GOSAT chlorophyll fluorescence, *Proc.*
8 *Biol. Sci.*, 280, 20130 171, <https://doi.org/10.1098/rspb.2013.0171>, 2013.
- 9 Magney, T. S., Bowling, D. R., Logan, B. A., Grossmann, K., Stutz, J., Blanken, P. D., Burns, S. P., Cheng, R., Garcia, M. A., Köhler,
10 P., Lopez, S., Parazoo, N. C., Raczka, B., Schimel, D., and Frankenberg, C.: Mechanistic evidence for tracking the seasonality of pho-
11 tosynthesis with solar-induced fluorescence, *Proceedings of the National Academy of Sciences of the United States of America*, 116,
12 11 640–11 645, <https://doi.org/10.1073/pnas.1900278116>, 2019.
- 13 Magney, T. S., Barnes, M. L., and Yang, X.: On the Covariation of Chlorophyll Fluorescence and Photosynthesis Across Scales, *Geophysical*
14 *Research Letters*, 47, <https://doi.org/10.1029/2020gl091098>, 2020.
- 15 Maguire, A. J., Eitel, J. U. H., Griffin, K. L., Magney, T. S., Long, R. A., Vierling, L. A., Schmiede, S. C., Jennewein, J. S., Weygint,
16 W. A., Boelman, N. T., and Bruner, S. G.: On the Functional Relationship Between Fluorescence and Photochemical Yields in Complex
17 Evergreen Needleleaf Canopies, *Geophysical Research Letters*, 47, <https://doi.org/10.1029/2020gl087858>, 2020.
- 18 Marrs, J. K., Reblin, J. S., Logan, B. A., Allen, D. W., Reinmann, A. B., Bombard, D. M., Tabachnik, D., and Hutya, L. R.: Solar-Induced
19 Fluorescence Does Not Track Photosynthetic Carbon Assimilation Following Induced Stomatal Closure, *Geophysical Research Letters*,
20 47, <https://doi.org/10.1029/2020gl087956>, 2020.
- 21 Monteith, J. L.: Solar Radiation and Productivity in Tropical Ecosystems, *Journal of Applied Ecology*, 9, 747–766, 1972.
- 22 Parazoo, N. C., Bowman, K., Fisher, J. B., Frankenberg, C., Jones, D. B., Cescatti, A., Perez-Priego, O., Wohlfahrt, G., and Montagnani,
23 L.: Terrestrial gross primary production inferred from satellite fluorescence and vegetation models, *Global change biology*, 20, 3103–21,
24 <https://doi.org/10.1111/gcb.12652>, 2014.
- 25 Reichstein, M., Falge, E., Baldocchi, D., Papale, D., Aubinet, M., Berbigier, P., Bernhofer, C., Buchmann, N., Gilmanov, T., Granier, A.,
26 Grunwald, T., Havrankova, K., Ilvesniemi, H., Janous, D., Knohl, A., Laurila, T., Lohila, A., Loustau, D., Matteucci, G., Meyers, T.,
27 Miglietta, F., Ourcival, J.-M., Pumpanen, J., Rambal, S., Rotenberg, E., Sanz, M., Tenhunen, J., Seufert, G., Vaccari, F., Vesala, T., Yakir,
28 D., and Valentini, R.: On the separation of net ecosystem exchange into assimilation and ecosystem respiration: review and improved
29 algorithm, *Global change biology*, 11, 1424–1439, <https://doi.org/10.1111/j.1365-2486.2005.001002.x>, 2005.
- 30 Schaaf, C. B., Gao, F., Strahler, A. H., Lucht, W., Li, X., Tsang, T., Strugnell, N. C., Zhang, X., Jin, Y., Muller, J.-P., Lewis, P., Barns-
31 ley, M., Hobson, P., Disney, M., Roberts, G., Dunderdale, M., Doll, C., d’Entremont, R. P., Hu, B., Liang, S., Privette, J. L., and
32 Roy, D.: First operational BRDF, albedo nadir reflectance products from MODIS, *Remote Sensing of Environment*, 83, 135–148,
33 [https://doi.org/10.1016/s0034-4257\(02\)00091-3](https://doi.org/10.1016/s0034-4257(02)00091-3), 2002.
- 34 Sellers, P. J.: Canopy reflectance, photosynthesis and transpiration, *International Journal of Remote Sensing*, 6, 1335–1372,
35 <https://doi.org/10.1080/01431168508948283>, 1985.
- 36 Sims, D. A., Brzostek, E. R., Rahman, A. F., Dragoni, D., and Phillips, R. P.: An improved approach for remotely sensing water stress impacts
37 on forest C uptake, *Global change biology*, 20, 2856–2866, <https://doi.org/10.1111/gcb.12537>, 2014.



- 1 Smith, W. K., Dannenberg, M. P., Yan, D., Herrmann, S., Barnes, M. L., Barron-Gafford, G. A., Biederman, J. A., Ferrenberg, S., Fox, A. M.,
2 Hudson, A., Knowles, J. F., MacBean, N., Moore, D. J. P., Nagler, P. L., Reed, S. C., Rutherford, W. A., Scott, R. L., Wang, X., and Yang,
3 J.: Remote sensing of dryland ecosystem structure and function: Progress, challenges, and opportunities, *Remote Sensing of Environment*,
4 233, 111401, <https://doi.org/10.1016/j.rse.2019.111401>, 2019.
- 5 Sun, Y., Fu, R., Dickinson, R., Joiner, J., Frankenberg, C., Gu, L., Xia, Y., and Fernando, N.: Drought onset mechanisms revealed by satellite
6 solar-induced chlorophyll fluorescence: Insights from two contrasting extreme events, *Journal of Geophysical Research: Biogeosciences*,
7 120, 2427–2440, <https://doi.org/10.1002/2015jg003150>, 2015.
- 8 Sun, Y., Frankenberg, C., Wood, J. D., Schimel, D. S., Jung, M., Guanter, L., Drewry, D. T., Verma, M., Porcar-Castell, A., Griffis, T. J.,
9 Gu, L., Magney, T. S., Kohler, P., Evans, B., and Yuen, K.: OCO-2 advances photosynthesis observation from space via solar-induced
10 chlorophyll fluorescence, *Science*, 358, <https://doi.org/10.1126/science.aam5747>, 2017.
- 11 Sun, Y., Frankenberg, C., Jung, M., Joiner, J., Guanter, L., Köhler, P., and Magney, T.: Overview of Solar-Induced chlorophyll Fluorescence
12 (SIF) from the Orbiting Carbon Observatory-2: Retrieval, cross-mission comparison, and global monitoring for GPP, *Remote Sensing of*
13 *Environment*, 209, 808–823, <https://doi.org/10.1016/j.rse.2018.02.016>, 2018.
- 14 Turner, A. J. and Jacob, D. J.: Balancing aggregation and smoothing errors in inverse models, *Atmos Chem Phys*, 15, 7039–7048,
15 <https://doi.org/10.5194/acp-15-7039-2015>, 2015.
- 16 Turner, A. J., Köhler, P., Magney, T. S., Frankenberg, C., Fung, I., and Cohen, R. C.: A double peak in the seasonality of California’s
17 photosynthesis as observed from space, *Biogeosciences*, 17, 405–422, <https://doi.org/10.5194/bg-17-405-2020>, 2020.
- 18 USDA: National Agricultural Statistics Service Cropland Data Layer: Published crop-specific data layer, [https://nassgeodata.gmu.edu/](https://nassgeodata.gmu.edu/CropScape/)
19 [CropScape/](https://nassgeodata.gmu.edu/CropScape/), 2018.
- 20 Veefkind, J. P., Aben, I., McMullan, K., Förster, H., de Vries, J., Otter, G., Claas, J., Eskes, H. J., de Haan, J. F., Kleipool, Q., van Weele,
21 M., Hasekamp, O., Hoogeveen, R., Landgraf, J., Snel, R., Tol, P., Ingmann, P., Voors, R., Kruizinga, B., Vink, R., Visser, H., and Levelt,
22 P. F.: TROPOMI on the ESA Sentinel-5 Precursor: A GMES mission for global observations of the atmospheric composition for climate,
23 air quality and ozone layer applications, *Proc SPIE*, 120, 70–83, <https://doi.org/10.1016/j.rse.2011.09.027>, 2012.
- 24 Wang, X., Dannenberg, M. P., Yan, D., Jones, M. O., Kimball, J. S., Moore, D. J. P., Leeuwen, W. J. D., Didan, K., and Smith, W. K.: Globally
25 Consistent Patterns of Asynchrony in Vegetation Phenology Derived From Optical, Microwave, and Fluorescence Satellite Data, *Journal*
26 *of Geophysical Research: Biogeosciences*, 125, <https://doi.org/10.1029/2020jg005732>, 2020.
- 27 Yang, H., Yang, X., Zhang, Y., Heskell, M. A., Lu, X., Munger, J. W., Sun, S., and Tang, J.: Chlorophyll fluorescence tracks seasonal variations
28 of photosynthesis from leaf to canopy in a temperate forest, *Global change biology*, 23, 2874–2886, <https://doi.org/10.1111/gcb.13590>,
29 2017.
- 30 Yang, X., Tang, J., Mustard, J. F., Lee, J.-E., Rossini, M., Joiner, J., Munger, J. W., Kornfeld, A., and Richardson, A. D.: Solar-induced chloro-
31 phyll fluorescence that correlates with canopy photosynthesis on diurnal and seasonal scales in a temperate deciduous forest, *Geophysical*
32 *Research Letters*, 42, 2977–2987, <https://doi.org/10.1002/2015gl063201>, 2015.
- 33 Yao, J., Liu, H., Huang, J., Gao, Z., Wang, G., Li, D., Yu, H., and Chen, X.: Accelerated dryland expansion regulates future variability in
34 dryland gross primary production, *Nature communications*, 11, <https://doi.org/10.1038/s41467-020-15515-2>, 2020.
- 35 Yin, Y., Byrne, B., Liu, J., Wennberg, P. O., Davis, K. J., Magney, T., Köhler, P., He, L., Jeyaram, R., Humphrey, V., Gerken, T., Feng,
36 S., Digangi, J. P., and Frankenberg, C.: Cropland Carbon Uptake Delayed and Reduced by 2019 Midwest Floods, *AGU Advances*, 1,
37 <https://doi.org/10.1029/2019av000140>, 2020.